ACSNANO

www.acsnano.org

ARTICLE

Coarse-Grained Simulations for the Characterization and Optimization of Hybrid Protein–DNA Nanostructures

Raghu Pradeep Narayanan,[▽] Jonah Procyk,[▽] Purbasha Nandi,[#] Abhay Prasad,[#] Yang Xu,[#] Erik Poppleton, Dewight Williams, Fei Zhang, Hao Yan, Po- Lin Chiu,* Nicholas Stephanopoulos,* and Petr Šulc*

Cite This: *ACS Nano* 2022, 16, 14086–14096

Read Online

ACCESS | Metrics & More | Article Recommendations | Supporting Information

ABSTRACT: **We present here the combination of experimental and computational modeling tools for the design and characterization of protein–DNA hybrid nanostructures. Our work incorporates several features in the design of these nanostructures: (1) modeling of the protein–DNA linker identity and length; (2) optimizing the design of protein–DNA cages to account for mechanical stresses; (3) probing the incorporation efficiency of protein–DNA conjugates into DNA nanostructures. The modeling tools were experimentally validated using structural characterization methods like cryo-TEM and AFM. Our method can be used for fitting low-resolution electron density maps when structural insights cannot be deciphered from experiments, as well as enable *in-silico* validation of nanostructured systems before their experimental realization. These tools will facilitate the design of complex hybrid protein–DNA nanostructures that seamlessly integrate the two different biomolecules.**

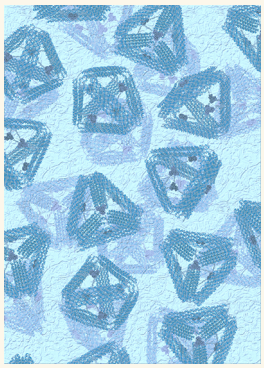

KEYWORDS: *DNA nanotechnology, protein–DNA, cryo-EM fitting, coarse-grained models, molecular dynamics*

INTRODUCTION

The field of DNA nanotechnology[1,2] has made great strides in bionanotechnology over the past three decades. It relies on using the predictable Watson–Crick base pairing[3] of oligonucleotides in order to assemble them into desired 2D and 3D shapes. The nano-objects thus formed have been utilized for a variety of applications, including molecular storage,[4,5] logic gate circuits,[6−9] and drug delivery machines.[10,11] Despite the tremendous progress the field has made in the past few decades, the limited chemical functionality of oligonucleotides has prevented DNA nanostructures from realizing many behaviors and interactions that proteins achieve in living organisms. One way to circumvent this limitation and construct more complex nanostructures—like "nano-robots" that can interact in a programmable way with biological systems—is to include functional protein units on a DNA scaffold. This approach has certain advantages compared with designing structures from amino acids alone: currently, *de novo* design[12] of protein nanostructures that rival the complexity of DNA origami is not possible, mainly because protein self-assembly lacks the predictability and orthogonal interactions inherent to nucleic acids. The most commonly used technique to design protein nanostructures revolves around the software Rosetta,[13] but this approach is still limited to experts in the field due to its complexity. Hence, despite impressive achievements in recent years, nanotechnology based on designed proteins has not yet achieved the level of versatility, structural complexity, and logic-gated control ability that has been developed for DNA nanotechnology.[14,15] Methods for the design and characterization of protein–DNA hybrid nanostructures,[16,17] however, still lag behind all-DNA structure design software like Tiamat,[18] CaDNAno,[19] Adenita,[20] and MagicDNA.[21] The design rules for hybrid nanomaterials have yet to be figured out completely, so most structures are designed in a heuristic and *ad hoc* fashion, and designer software and simulation methods integrating both DNA and protein nanostructures have only started to be developed recently.[20,22] In this work, we aim to provide efficient tools for the design and verification of hybrid

Received: April 24, 2022
Accepted: August 15, 2022
Published: August 18, 2022

https://doi.org/10.1021/acsnano.2c04013
ACS Nano 2022, 16, 14086–14096

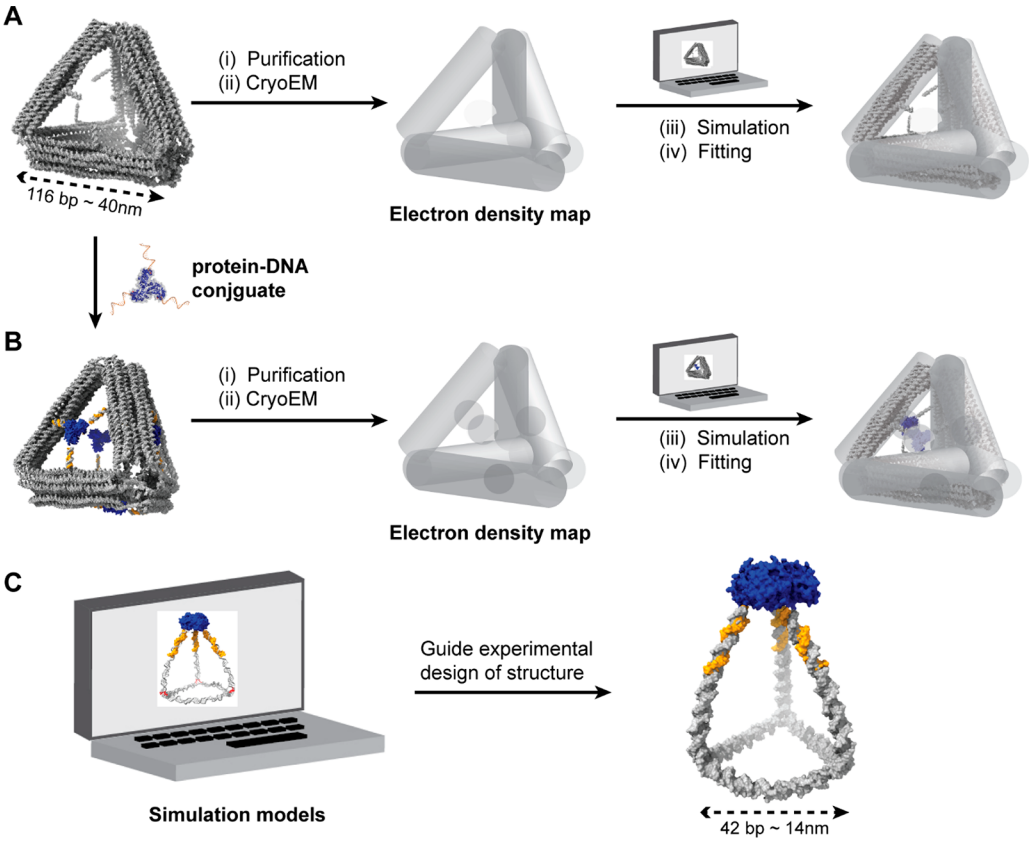

Figure 1. Using computational simulations to guide protein−DNA cage design. Elucidating the cryo-EM density map of the empty tetrahedral origami cage (A) and the origami with the trimeric protein incorporated (B), then using the density map to fit the simulated models to find the best correlation. (C) Simulating a protein−DNA tetrahedral cage (PDTet) in order to predict the optimal design.

nanostructures in conjunction with experimental characterization.

In order to scale up protein−DNA nanostructure design and synthesis, basic building blocks and model systems still need to be designed and fully characterized. Designs utilizing DNA-binding proteins have shown impressive and tantalizing results in this direction,[17] but they severely limit the protein functionality that can be incorporated into the design. For example, a given protein of interest would have to fuse to a DNA-binding domain, which increases the molecular weight by a nontrivial amount and could affect the presentation of the final protein if a flexible linker is used. Furthermore, DNA-binding proteins interact with oligonucleotides in a reversible manner, so even with dissociation constants in the nanomolar regime there could be protein detachment under the nanomolar concentrations used with many DNA origami nanostructures. We instead focus on chemically conjugating desired proteins to DNA in a site-specific manner, followed by hierarchical incorporation of these building blocks into DNA structures bearing complementary handles. Covalent conjugation is generally irreversible, and direct attachment to a DNA handle allows for a high degree of orthogonality due to Watson−Crick pairing. Furthermore, DNA strands can be attached to any point on a protein surface (by introducing a suitable reactive amino acid), whereas DNA-binding proteins must be fused to one of the two protein termini.

Understanding the design of these building blocks, and how they can best form hybrid nanoassemblies, requires us to have insight into various molecular parameters: (1) the ideal site for DNA conjugation on the protein; (2) the choice of chemical bioconjugation reaction used; (3) the flexibility and length of the small molecule linker between the DNA backbone and the protein surface. Once a protein−DNA building block has been synthesized, incorporating it into a hybrid system presents a distinct challenge. Often, the incorporation efficiency of the conjugate into the nanostructure is low, and it may not be immediately clear why this is the case. Possibilities include the misincorporation of complementary DNA handle sites, unintended steric and electrostatic clashes, or mechanical strain experienced by the hybrid nanostructure. To efficiently synthesize next-generation systems it will be critical to model the composite, *integrated* nanostructure, and take into account the properties of both the DNA and protein components, as well as the linkers that join them. In order to address these challenges and work toward design principles for these nanostructures, we used our recently developed protein−DNA hybrid model to characterize experimental results and optimize the design of two protein−DNA cage systems (Figure 1). In particular, we use a trimeric protein−DNA building block based on the KDPG aldolase building block reported by the Stephanopoulos lab in a previous report.[23]

The ability to construct defined three-dimensional cages with protein "walls" will yield applications in drug delivery (e.g., "artificial viruses"), novel vaccine platforms, or synthesis of enzymatic nanoreactors. Toward this end, we first explored integrating the KDPG aldolase-DNA conjugate into a tetrahedral DNA origami cage using three complementary handles on each of the four faces of the cage (Figure 1A,B). We chose this system in order to (1) gain structural insights into protein−DNA hybrids of large size (>14,000 nucleotides)

https://doi.org/10.1021/acsnano.2c04013
ACS Nano 2022, 16, 14086−14096

by both simulation and experiment, (2) simulate the chemical linker between the protein and DNA handle and investigate the flexibility of the origami design, and (3) demonstrate the applicability of our methods in characterizing DNA nanostructures by cryogenic transmission electron microscopy (cryo-EM). Our modeling approaches are based on two tools that we recently developed: a coarse-grained model of DNA and proteins, called ANM-oxDNA,[24] and the OxView design tool,[25] originally developed for DNA nanostructures but since extended to support visualization and editing of protein−DNA nanostructures.[19] Additionally, we extended the online simulation server, oxDNA.org[26] to support ANM-oxDNA simulations and performed many of the simulations in this paper as part of that service, which we make freely available to the community for *in-silico* testing and verification of protein−DNA hybrid designs. We first designed a DNA origami tetrahedral cage with four available triangular void spaces for incorporating the KDPG aldolase-DNA conjugate (Figure 1A,B). This cage was characterized by cryo-EM to obtain an electron density map by single-particle reconstruction, and the density was fit with a mean structure obtained from coarse-grained simulations to verify that our models can correctly capture the hybrid nanostructure shape and structure.

In parallel, we applied our simulation model to a different assembly: a tetrahedral protein−DNA cage, with the aldolase capping a wireframe structure with six edges of four DNA helical turns each. We term this structure the protein−DNA tetrahedron (PDTet) (Figure 1C). This structure formed with only modest yield in our initial publication reporting its design and synthesis.[23] We thus asked whether the simulation could provide insight into this low efficiency and suggest modifications to the structure design that would improve successful formation. Crucially, this system could also probe whether our computational model could be applied to hybrid nanostructures where, unlike the larger origami cage, the protein comprises a significant fraction of the assembly. We especially note that with PDTet, the final structure does not form in the absence of the protein vertex, and the homotrimeric protein−DNA conjugate is necessary for helping "fold" the triangular base into a wireframe cage. We simulated different PDTet structures with a varying number of unpaired polythymidine residues at the vertices of this nanostructure and experimentally optimized the yield of structure formation (as visualized by AFM) by tuning the flexibility at these sites.

RESULTS AND DISCUSSION

To probe the assembly of the hybrid protein-origami cage, we first synthesized the homotrimeric aldolase protein−DNA building block (PDNA) according to the previous report[23] and as described in the Methods section below. With this purified building block in hand, we proceeded to attach it to the four sides of the tetrahedral origami cage.

Design and Synthesis of the Tetrahedral Origami Cage with PDNA Incorporated. The origami cage was designed using the software Cadnano,[19] with each arm consisting of 10 helices arranged on a honeycomb lattice. We opted for a tetrahedral geometry in order to avoid the preferred orientation problem that often hinders single-particle cryo-EM reconstruction.[27] The details of the origami design can be found in Figure S7. Each side was designed to have a length of 35 nm. The handles for the incorporation of the PDNA were positioned in such a way that one conjugate would bind onto each of the four faces of the tetrahedron, giving a maximum of four aldolase trimers per structure. In designing this nanostructure, we incorporated flexibility at the vertices of the tetrahedral cage by introducing polythymidine linkers (5 to 11 dT residues) to promote efficient formation. These samples were subjected to agarose gel electrophoresis (AGE), followed by excision of the desired band, elution of the origami, and verification of its structure by negative-stain EM (Figures S7 and S8). From the AGE analysis (Figure S7C), we concluded that the 11T version gave the best yields, so the rest of our studies were performed using this version of the cage. After visual confirmation by negative-stain EM, the purified origami cage was plunge-frozen (sections S2 and S3) and characterized by cryo-EM (Figure 2A). Images were processed

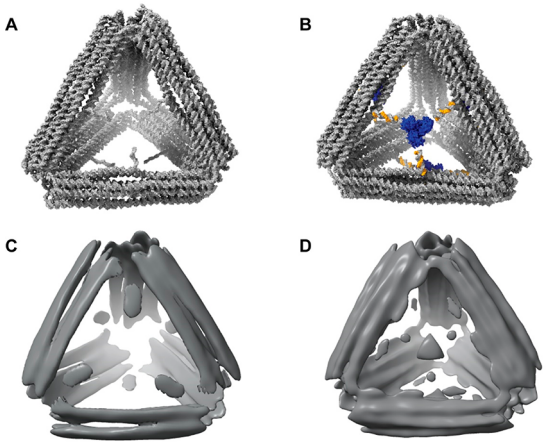

Figure 2. Cryo-EM reconstruction of tetrahedral origami cages. (A) Schematic of the empty origami cage. (B) Schematic of the origami cage incorporating PDNA. (C) Cryo-EM reconstruction of (A) at 26 Å. (D) Cryo-EM reconstruction of (B) at 28 Å.

(section S4 and Figure S10) using RELION 3.0 (Figure 2C). After characterizing the empty cages, we proceeded to probe the formation of the cage incorporating PDNA.

The PDNA-bearing cages (Figure 2B) were synthesized as described in section S2. The samples were first characterized by negative-stain EM and then by cryo-EM (Figure S11) as before. The resulting reconstruction (Figure 2D, Figure S11) shows a clear electron density in the center of each face, supporting the incorporation of protein into the tetrahedral frame. These maps were later used to validate the ability of our coarse-grained model to correctly capture the experimentally determined structure.

Simulation Development for Protein−DNA Hybrid Systems. To characterize the cages with the PDNA incorporated, we developed a molecular simulation pipeline. Our ultimate goal is to provide tools and methods that aid in the nanostructure design and validation process *in silico*, thus speeding up the development of novel designs, as well as offloading part of the process to computational modeling. Ideally, one would like to simulate and model protein−DNA hybrids at atomistic resolution. However, the system sizes (up to several tens of thousands of base pairs) and long time scales required for the characterization of such nanostructures present an enormous challenge. As a result, coarse-grained models have become increasingly more popular in nucleic acid nanotechnology. We used a recently introduced protein−DNA hybrid model,[24] based on the oxDNA coarse-grained model of DNA.[28−31] This model was previously used to study a wide

https://doi.org/10.1021/acsnano.2c04013
ACS Nano 2022, 16, 14086−14096

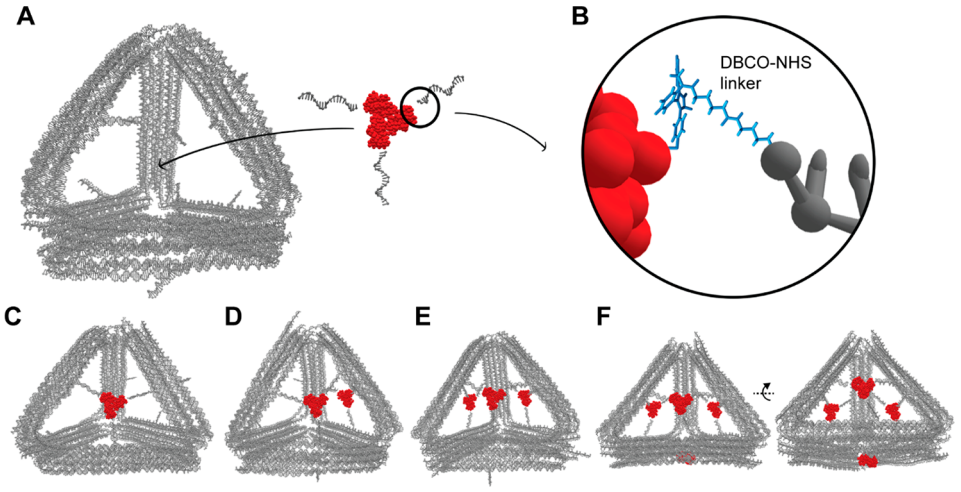

Figure 3. (A) Schematic of PDNA incorporation in simulation models, using the empty cage mean structure at low temperature (113 K). (B) Atomic model of the DBCO-NHS ester linker, which is represented by a spring potential in the simulation. (C−F) Mean structures of origami bearing 1−4 PDNA building blocks, respectively, at low temperature conditions. Panel F includes a second view of the model with 4 PDNA incorporated so that the bottom protein is visible.

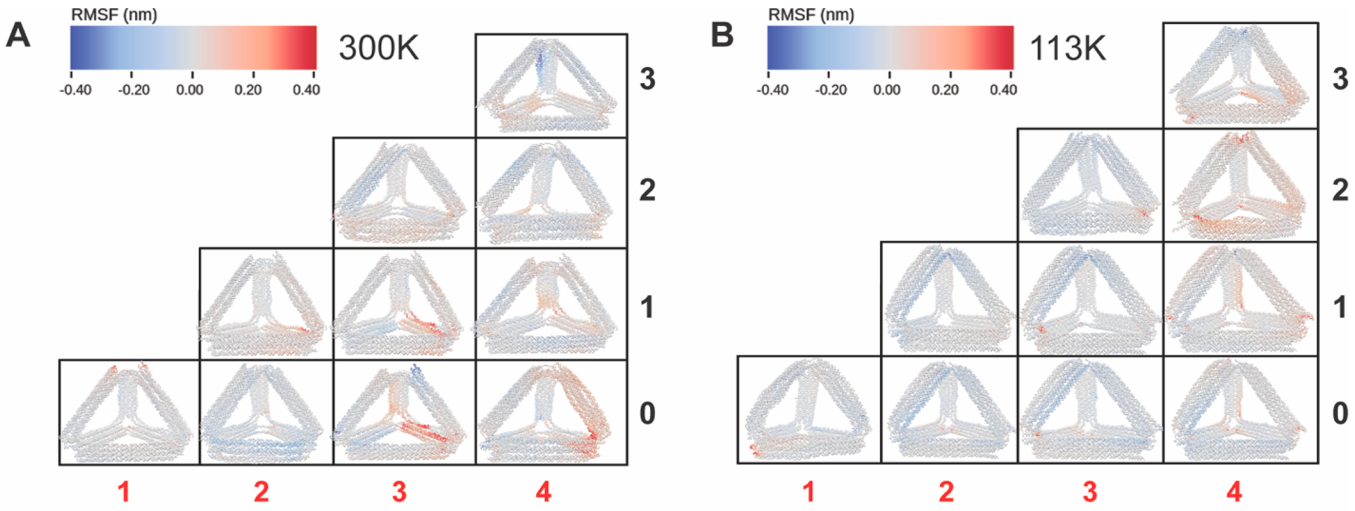

Figure 4. PDNA effect on cage flexibility. Difference in RMSF between the column model (red index denoting the number of PDNAs incorporated) and row model (black index denoting the number of PDNAs incorporated). RMSF differences are calculated as the column model RMSF minus the row model RMSF. Differences are displayed on the simulation mean structures of the row index with (A) being the relative differences in RMSF between all high temperature (300 K) simulation models and (B) being the relative differences in RMSF between all low temperature mean structures (113 K). The incorporated PDNA is not shown in the mean structures, as the RMSF was calculated only using the DNA component of the DNA−protein hybrid nanostructure.

range of DNA nanostructures and devices and could reproduce their thermodynamics, mechanical properties, and kinetics.[28−31] To incorporate proteins, the oxDNA model was extended with an Anisotropic Network Model[32] (ANM) that represents the polypeptides as beads connected by springs, parametrized to per residue fluctuation data—i.e., crystal B factors or a fully atomistic simulation trajectory—in order to capture the basic fluctuations and flexibility of the protein. Using the ANM-oxDNA model, we investigate how differences in protein incorporation and spacer length affected the mechanical properties of the DNA nanostructures and compared our results to those obtained experimentally.

Simulation of the Tetrahedral Origami Cages. The Cadnano design of the DNA origami was first converted into oxDNA using tacoxDNA[32] and further modified using our design tool oxView,[25] which was extended to also support protein representations for nanostructure design.[19] Modifications were made to include 11T spacers at the origami vertices and to add handles for the incorporation of the PDNA. Five different simulation models were made by first parametrizing an ANM to the PDNA protein KDPG and subsequently adding the ANM to each model according to its PDNA incorporation. To finish the preparation of the simulation models the ANM was parametrized, the linker was introduced, and the simulation topology relaxed as stated in the Methods section. Ten total simulation systems were prepared using each of the five models with different PDNA incorporation at 1 M salt concentration with two different temperatures: (1) 300 K ("high temperature") and (2) 113 K ("low temperature"). Figure 3B shows the atomic model of the DBCO-NHS ester linker represented by a spring potential. Figure 3 panels A and C−F show the mean structures for the different PDNA-bearing

https://doi.org/10.1021/acsnano.2c04013
ACS Nano 2022, 16, 14086−14096

tetrahedral cages at low-temperature conditions. For our production simulations, each of the ten systems was simulated for 1×10^9 molecular dynamic simulation steps or approximately 3 μs.

Simulation Results for the Tetrahedral Protein Origami Cage. To characterize the differences between systems with different numbers (1−4) of protein trimers incorporated, we first analyzed the effect of adding PDNA on the origami cage flexibility, given that the protein trimer effectively cross-links the three arms of the face it binds to. By comparing the root mean squared fluctuations (RMSF) of each model's identical DNA cage, we can see how the addition of the PDNA to the system affects the flexibility of the tetrahedral cage at the individual nucleotide level.

Figure 4 depicts the difference between the RMSF values for each pair of simulation models with differing number of PDNA incorporation, calculated per nucleotide as the column model's RMSF minus the row model's RMSF. Both the mean structure and RMSF of each model's DNA cage were averaged over the simulation trajectory using the oxDNA analysis tools.[25] Higher (red) values indicate an increase in flexibility in the structure, while lower (blue) values indicate an increase in rigidity. In both conditions (high and low temperatures) the PDNA caused a clear decrease in the RMSF values of the arms with occupied handles. The decrease in RMSF corresponds to a local increase in rigidity, arising from the cross-linking by the PDNA (via the DNA handles) of the scaffold of the DNA origami. However, the addition of each subsequent PDNA introduces additional pulling forces on the adjacent faces, resulting in an increase of flexibility in arms that have *both* DNA handles bound by PDNA building blocks. This perhaps counterintuitive result can be explained by the pulling forces of the proteins disrupting some of the stacking interactions along the ten-helix bundle arm, thereby causing an increase in flexibility.

Beyond RMSF, differences in the mean structures suggest that the PDNA has a rigidifying effect on the face of the DNA cage to which it is attached. The mean structure for four PDNAs incorporated shows a significant change in the origami curvature, as evidenced by its straighter arms relative to all other mean structures. Figure 3 panels A and F depict the mean structures of the bare origami and the four-PDNA mean structures at low-temperature conditions, where the largest difference in curvature can be observed.

Mean structures from each simulation trajectory were compared to the experimentally generated cryo-EM maps of the tetrahedral cage and PDNA-incorporated tetrahedral cage with the resulting fits shown in Figure 5. The mean structure files were stripped of their protein and DNA handles to avoid biasing the fitting, and the structures were exported from a coarse-grained nucleotide-level representation to a fully atomistic PDB format. Using UCSF Chimera,[33] the volume maps of the mean structures were generated from the atomic coordinates and fit to the experimental cryo-EM maps at 27 Å for both cryo-EM maps.

The generated density from the atomic model (translucent pink in Figure 5) closely fit the experimental maps (blue in Figure 5). The PDNA density in the cryo-EM map matched its position in simulation and confirmed the PDNA incorporation. These results corroborate that our coarse-grained model can indeed fit the cryo-EM map. We then analyzed the fittings to determine whether the slight differences in curvature between the cryo-EM maps could indicate the preferred level of incorporation of PDNA into the system.

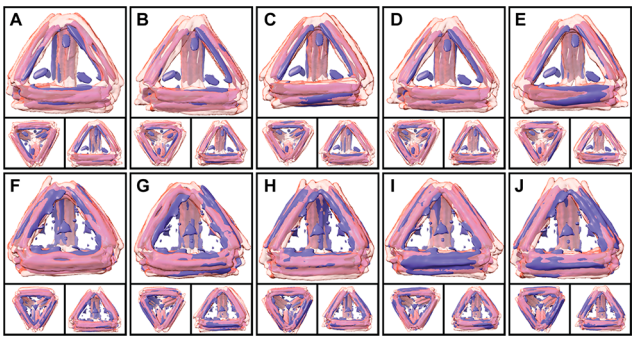

Figure 5. Fitting cryo-EM maps with mean structures obtained from the simulations at 300 K. The densities generated from the mean atomic models at the same resolution as the cryo-EM map are shown in translucent pink and the cryo-EM map itself shown in purple. Each subfigure depicts three views of the same fitting. (A) 0 PDNA fit to empty cage. (B) 1 PDNA fit to empty cage. (C) 2 PDNA fit to empty cage. (D) 3 PDNA fit to empty cage. (E) 4 PDNA fit to empty cage. (F) 0 PDNA fit to filled cage. (G) 1 PDNA fit to filled cage. (H) 2 PDNA fit to filled cage. (I) 3 PDNA fit to filled cage. (J) 4 PDNA fit to filled cage.

Unfortunately, the resolution of the obtained cryo-EM map of the hybrid nanostructure was not sufficient to distinguish the difference between the models with different number of PDNA incorporated. The bulk assay, and low-resolution nature of the cryo-EM maps, combined with the subtle differences between models, made it impossible to determine a preference for PDNA incorporation from minor deviations in curvature. The correlation coefficients for fitting and associated images for both the filled and empty cryo-EM maps are available in section S8.

Fluorophore Assay for Determining the Number of Proteins per Cage. Because our reconstruction was performed with a small data set and was reconstructed with a tetrahedral symmetry, we wanted to probe PDNA incorporation in a cost-effective and more dispositive way than cryo-EM experiments. For this we carried out a fluorophore-based assay, wherein the PDNA was synthesized using a DNA handle with a FAM dye at the 5′ end (Figure 6A) and the origami structure included a Cy5 dye. Then we proceeded to use fluorescence to elucidate the average number of proteins bound to the tetrahedral frame.

For this, we first obtained a calibration curve using known concentrations of the Cy5 handle strand and a FAM-labeled PDNA (Figure 6C). We made sure to perform these experiments using double-stranded DNA-dye conjugates to better match the experimental system, where the protein is attached to the cage through hybridized handles. We then made our PDNA-incorporated tetrahedral cage as before and obtained emission values for this sample at the respective emission wavelengths (Figure 6B). We used the calibration curves to obtain the concentrations of the sample, yielding values of 3.59 nM for the tetrahedral frame and 11.33 nM for PDNA, corresponding to ∼78.9% protein incorporation (assuming four possible proteins), or ∼3 proteins per cage on average.

We next turned to a different nanostructure, where PDNA is used as a structural building block. PDTet (Figure 1C) was chosen for this purpose for several reasons: (1) PDNA act as a critical structural building block to form a closed nano-

https://doi.org/10.1021/acsnano.2c04013
ACS Nano 2022, 16, 14086−14096

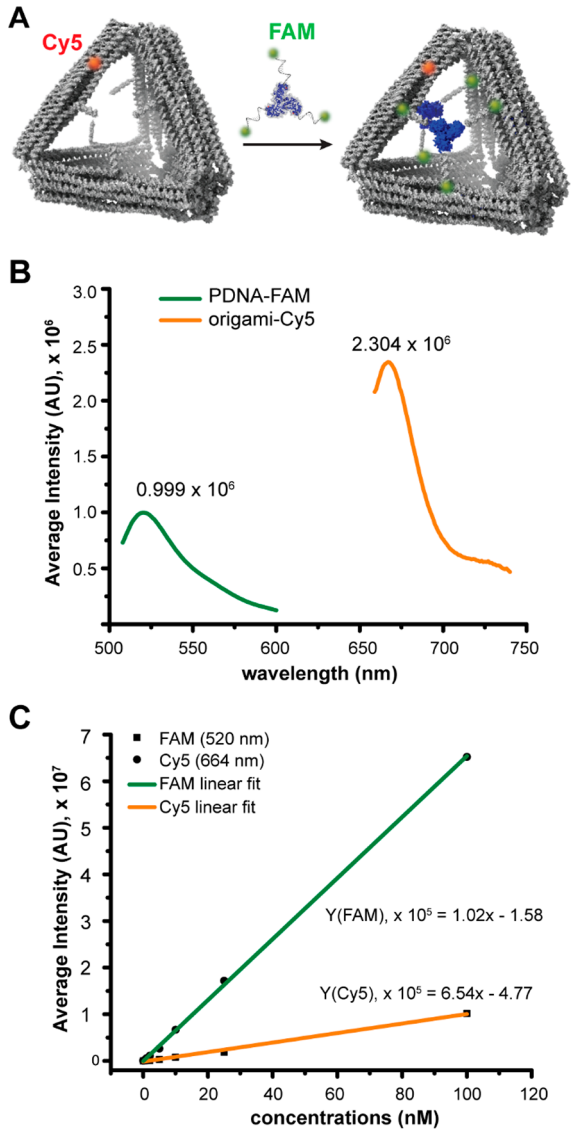

Figure 6. Fluorophore assay. (A) Schematic showing the design of the assay. (B) Fluorescence spectra of the PDNA-FAM and origami-Cy5. (C) Calibration curve obtained from using known concentrations of double stranded DNA-dye conjugates (either FAM or Cy5).

structural cage, and (2) experimental characterization of the system can be realized using AFM, a technique less time and cost intensive than cryo-EM. We started out by simulating different PDTet structures (Figure 7) having a varying number of polythymidines at the vertices of the nanostructure.

Simulation-Based Predictions of PDTet Assembly Yield. The experimental yields of hybrid DNA−protein nanostructures rely on a number of factors, many of which are system-specific. For our PDTet cage system, a key concern is the flexibility of the DNA cage arms—i.e., their ability to bend upward and form base pairs between the handles on the PDNA—and the resulting strain on the DNA cage when the structure is fully formed. By assessing these features, we aimed to predict the relative yields of each cage design as we introduced unpaired thymidine residues at the three vertices of the triangular DNA base structure.

Simulation files of the protein−DNA cage were prepared by first converting the Tiamat design of the origami cage with 3T

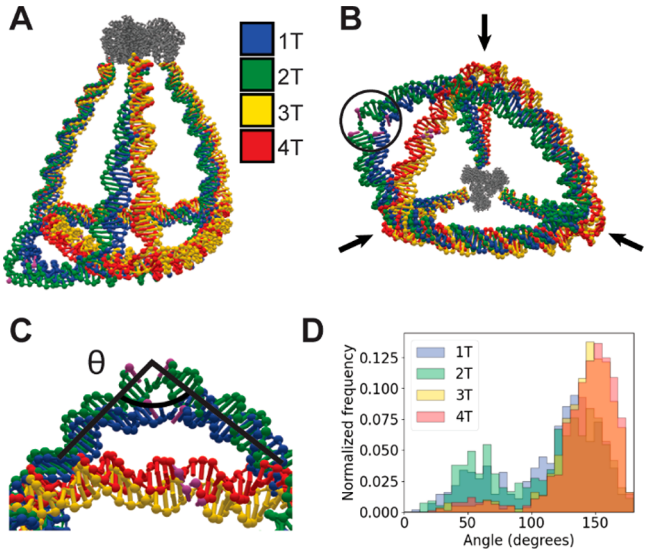

Figure 7. Simulating PDTet cages with varying linkers at the corners. (A, B) Two views of the aligned mean structures for cages with 1T, 2T, 3T, and 4T spacers, superimposed on one another. Arrows in (B) indicate the location of the thymidine spacers, and the circle in (B) indicates the nick point for the 1T and 2T models. (C) Depiction of angle measured across the nick point (Figure S12A). (D) Angle distribution in (C) across all four simulation trajectories.

spacers at the vertices into oxDNA via TacoxDNA.[32] Variations of this same cage with a different number of T spacers were created and relaxed (Methods) using oxView. All versions of the cage were simulated using molecular dynamics (1×10^9 steps; ~3 μs) at 300 K with 1 M salt concentration. Each cage was also simulated while attached to the same high temperature ANM representation of the aldolase protein used for the larger tetrahedron.

The aligned mean structures show significant differences in the DNA cage curvature depending on the number of T residues in the spacers in the vertices (Figure 7A,B). At the site of the nick in the base of the DNA cage, the 1T and 2T structures show a bend in one arm (Figure 7A−C), which is a mix of bent and straight arm configurations in the mean calculation. As more T residues are introduced into the spacers, the bent arm configurations are visited less often. Measuring the angle distribution between one side of the nicked helix to the other side of the nicked helix (Figure 7C) over the entire simulation trajectory illustrates the topological differences between varying the number of T spacers (Figure 7D). The configurations in Figure 7D with angles from 100 to 180° are considered "straight-arm" configurations, whereas angles 20−90° are considered "bent-arm" configurations. The key difference between the two populations is the ability of the nucleotides across the nick to maintain a coaxial stacking interaction. The disruption of this interaction is caused by mechanical strain induced on the base from the incorporation of the PDNA and the geometrical restrictions it imposes on the final hybrid structure.

Measuring the average energy of the two nucleotides before and after the nick in the DNA structure (section S7 Table S3) and comparing to simulations of the DNA structure without the protein—i.e., the triangular base with the single-stranded complementary arms (section S7 Table S4)—elucidate an energetic penalty stemming primarily from the disruption of

https://doi.org/10.1021/acsnano.2c04013
ACS Nano 2022, 16, 14086−14096

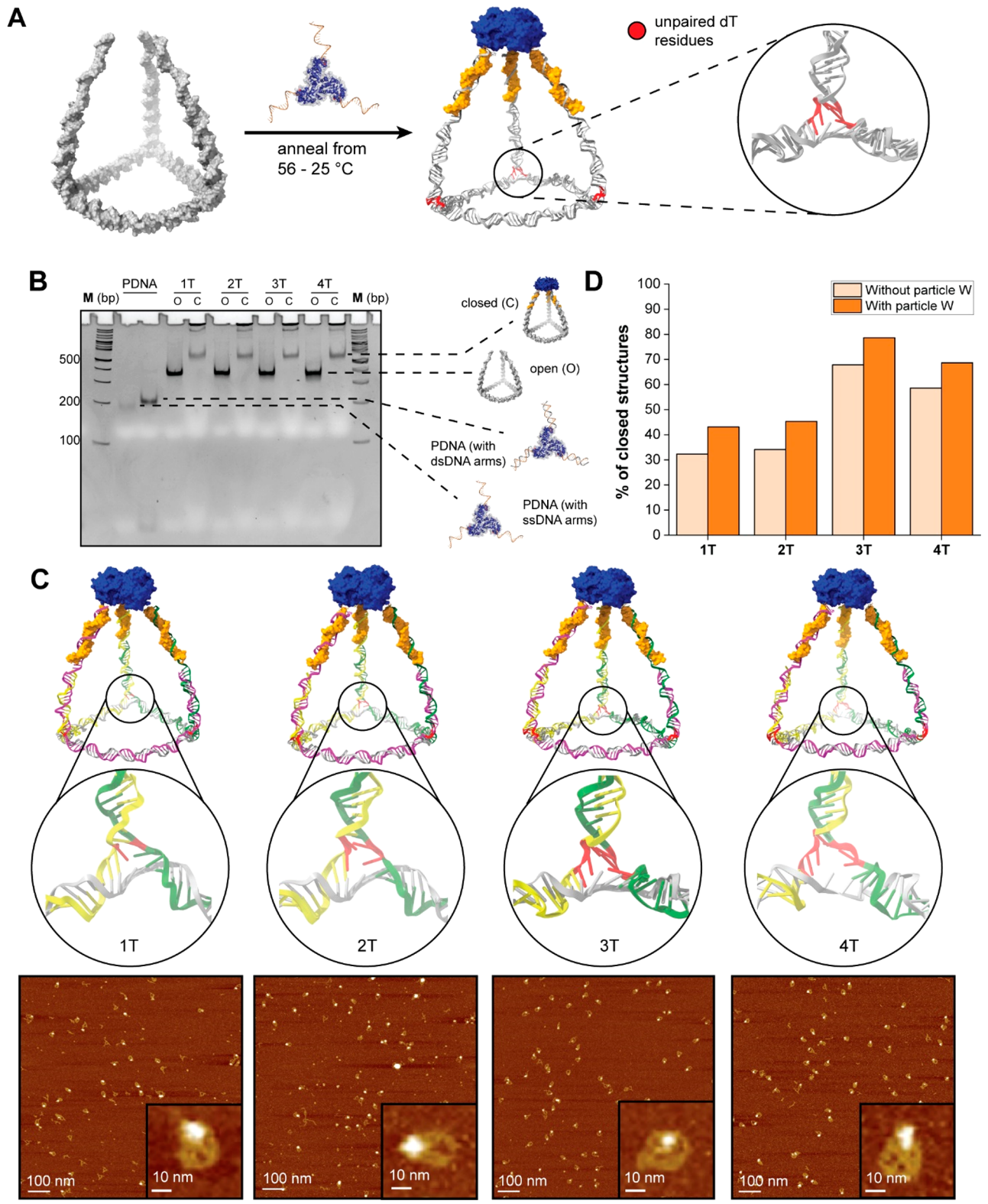

Figure 8. Experimental characterization of four-turn protein−DNA tetrahedral cages. (A) Schematic showing the formation of the hybrid nanostructure by the addition of the PDNA, including the location of unpaired poly dT residues (shown in red). (B) Native PAGE analysis of the open and closed tetrahedrons with varying number of poly dT residues, alongside controls of the single and double stranded versions of the PDNA. The PDNA is hard to visualize when the handles are single-stranded (lane 2), so the complementary strand was added to improve the staining (lane 3). (Lane M: 100 bp dsDNA ladder). (C) Schematic versions of the PDTet cages (1T, 2T, 3T and 4T) with their zoomed in detail showing the variations at the vertices. Below each image are AFM images to illustrate hybrid structures. (D) Bar plot of the percentage of well-formed PDTet cages, as analyzed from AFM images (with and without particles W means the with/without the inclusion of ambiguous particles as described in section S3 and Figures S21−24).

https://doi.org/10.1021/acsnano.2c04013
ACS Nano 2022, 16, 14086−14096

the coaxial stacking and hydrogen bonding of the nucleotides at the nick in the bent configurations. The trend in energy (section S7 Table S3) demonstrates that adding more dT nucleotides to the spacer mitigates this energetic penalty. However, the 3T model had more slightly more favorable coaxial and cross stacking interactions than the 4T model. Energy differences averaged over the T spacer nucleotides in each model were also examined. The same trend—i.e., lower average energy with increased length of T spacers—was observed, with the primary cause being a more favorable stacking interaction (S7 Table S1). This trend was not observed in simulations of the triangular base alone (S7 Table S2).

Overall, the aligned mean structures and energetic penalties incurred by the T spacer and nick nucleotides indicate that the strain in the structure decreases with increasing T spacer incorporation. From the above analysis, we can hypothesize that the 3T and 4T variants will have higher relative assembly yields, as they avoid the energetic penalties of the 1T and 2T variants. The slightly less favorable energy at the nick point (Figure S12A) of the 4T variant could indicate that this species will not form as well as the 3T.

To further explore the positional dependence (by individual arm) of T spacer incorporation, two sets of asymmetric cages were designed. One set of asymmetric systems was created by holding the arm across from the nick point constant as a 2T spacer and varying the T spacers in the other two arms of the DNA cage to have either 1T, 3T, or 4T spacers. Respectively, these designs were named 1.1, 1.3, and 1.4. The second set of asymmetric systems was created by holding the two arms attached to the nick point constant at 2T spacers and varying the T spacer amount of the one arm across from the nick point to have either 1T, 3T, or 4T spacers. Respectively, these designs were named 2.1, 2.3, and 2.4. All six asymmetric designs were relaxed, equilibrated, and simulated using the same exact methodology as the symmetric cages.

Figure S5 depicts the mean structures and accompanying nick point angle distributions for all six designs. As expected, the nick angle distribution is significantly affected by altering the two arms attached to the nick point and much less so for altering the arm across from the nick point. Raising the T spacer content of the two arms attached to the nick results in the cage visiting a bent configuration less often with a lower average energy at the nick due to more favorable stacking, cross stacking, and coaxial stacking interactions (Table S6). Alternatively, raising the T spacer content at the arm across from the nick point resulted in a marginally larger population of bent configurations and less favorable stacking, cross stacking, and coaxial stacking interactions at the nick (Table S10).

Assessing the average energy of the T spacers in the individual arms reveals some interesting trends. In designs that varied the two arms connected to the nick point, the left arm's (when viewed with the nick point in front and arm held constant in the back) average energy stays very similar across designs due to compensatory effects of a more favorable stacking interaction but less favorable cross stacking and coaxial stacking interactions (Table S8). The right arm's average energy has the same trade-off of stacking vs cross stacking and coaxial stacking interactions but has a significantly lower average energy due to a stronger stacking interaction (Table S9). The T spacers in the arm across from the nick (held constant at 2T spacers) showed a more favorable stacking interaction with increasing T spacers in the other 2 arms (Table S7). In designs that held the two arms connected to the nick constant, the left and right arms showed almost identical trends of a slightly more favorable stacking interaction with increasing T spacer number in the arm across from the nick (Table S11 and S12). The arm with the increased number of T spacers, however, showed no clear pattern in the average energy. Though not tested experimentally in this work, we would expect similar yields to their symmetric cage counterparts, in designs that hold the arm across from the nick point constant. Conversely, designs with two 2T arms and altering the arm across from the nick point may result in poorer yields compared to the symmetric 2T cage due to the slight promotion of bent configurations with increasing T spacer nucleotides in the altered arm.

Experimental Validation of T Spacer Effect on Protein−DNA Cage Assembly. Given the simulation predictions above, we sought to probe the effect of the dT linker on cage assembly via experiments. To form the cages, we first mixed the component oligonucleotide strands and assembled the triangular DNA structures with varying linkers (1T, 2T, 3T, and 4T), without the PDNA attached to it, as described in Supporting Information section S2. We characterized the system by native PAGE, extracted the band of interest and confirmed that the triangular structure formed via AFM, as shown in Figures S13−16. We then added the aldolase PDNA to these triangular structures, annealed them as described in section S2, and analyzed again by native PAGE (Figure 8B). The bands showed a significant shift from their open counterparts, indicating successful formation of the protein−DNA tetrahedral cages. To confirm nanostructure formation, we visualized the samples via AFM, examining both the crude samples (Figure S17−20) and the samples after gel extraction of the desired band (Figure 8C). Similar to the previous report,[23] we saw a varying fraction of cages that clearly corresponded to the four-turn tetrahedron with a protein vertex. We manually counted structures in the AFM images to determine the approximate yields of cage formation (Figures S21−24), with the results plotted in Figure 8D. It was apparent that the 3T version formed the best with a yield of 67.8% (or 78.6% if we include particles that may be cages but could not be unambiguously assigned as such in the images). The 4T version was the next best at 58.6% (68.67%), followed by a significant drop in yield for the 2T version at 34.11% (45.29%) and 1T at 32.3% (43.08%). This result tracks well with the predictions from our simulation and suggests that coarse-grained modeling can indeed be used to probe the relative stability of various protein−DNA nanostructure designs. We suggest that this interplay between simulation and experiment will be especially critical for more complex protein−DNA nanostructures, and guide the choice of DNA sequence/length, linker design, site of protein−DNA conjugation, and choice of protein building block.

CONCLUSIONS

In this work, we successfully elucidated a low-resolution cryo-EM density map for the tetrahedral DNA origami cage, both with and without the PDNA attached to it. We simulated models ranging from zero to four proteins in the origami cage and fit our experimental data to this model. Although the correlation factors could not give us an exact insight into the incorporation efficiency, we could determine an average number of three proteins per cage using a fluorophore assay.

https://doi.org/10.1021/acsnano.2c04013
ACS Nano 2022, 16, 14086−14096

We also simulated protein−DNA hybrid wireframe cages and found that the mechanical strain in the DNA wireframe nanostructures after the PDNA incorporation plays a critical role. Future hybrid nanostructure designs can be guided by our coarse-grained model, e.g., by suggesting linker incorporation (such as unpaired thymidines), changing the DNA handle length, or selecting a different protein building block in order to minimize these strains. In this way, the simulations can reduce the number of designs that have to be tested experimentally, as well as reveal shortcomings of the initial design that might not be trivial to solve by simple trial-and-error experimental design.

Going forward, the computational model can be improved by more explicitly incorporating protein−DNA interactions (e.g., electrostatics), as currently our tools rely solely on user-specified interactions, like a linker attaching the protein to the DNA. However, given the presence of cationic patches on many proteins, nonspecific electrostatic interactions with DNA could play a role in more complex designs. Proteins could also have unintended interactions with DNA through the presence of hydrophobic patches, which could for example interact with the blunt ends of helices or nick sites in DNA duplexes. Furthermore, sequestering multiple proteins in close proximity on a DNA nanoscaffold could result in enhanced, nonspecific aggregation between them due to the high effective concentration. Nevertheless, despite these limitations, we have demonstrated a protein−DNA simulation tool that can guide the design of hybrid nanostructures, including the explicit incorporation of linker models. We foresee the use of this model in designing a range of protein−DNA nanosystems, especially when the protein plays a key structural role in the final assembly. The script to convert PDNA structures from oxView to PDB format is available at https://github.com/lorenzo-rovigatti/oxDNA/tree/master/analysis, along with tools to produce mean structures and quantify their flexibility. Furthermore, we have made the ANM-oxDNA model freely available on our public GPU Web server, oxDNA.org, to make this resource easily accessible to the bionanotechnology community. The interactive design that supports design of DNA and protein nanostructures, as well as setting up ANM-oxDNA simulations, has been implemented in oxView tool, available at oxview.org and https://github.com/sulcgroup/oxdna-viewer. The structures designed in this work are available in nanobase.org, an online repository of nanostructures.[26]

METHODS

Synthesis of KDPG Aldolase Protein−DNA Building Blocks (PDNAs). As previously reported,[23] the PDNA was synthesized by expressing and purifying KDPG aldolase protein containing the noncanonical amino acid 4-azidophenylalanine (azF) at position 54 (the E54(azF) mutant). The purified KDPG aldolase was conjugated to a 21-base single-stranded DNA (ssDNA) strand via strain-promoted azide−alkyne click chemistry. The dibenzylcyclooctyne-(DBCO) modified DNA was synthesized by conjugating an amine modified DNA strand with a DBCO-sulfo(NHS) ester conjugation as previously reported.[17] This conjugate was used for both the tetrahedral cages reported here. The same procedure was used for synthesizing the FAM-modified PDNA as well (described in the fluorophore assay section), where the strand used for conjugation to the protein was purchased from IDT having a FAM modification at the 5′ end. The sequence of the strand attached to the protein is (5′ to 3′):(5AmMC6)TGAGTTCCGTCAGGTCTGCTC.

Parameterization of KDPG Aldolase Anisotropic Network Models. To approximately mimic the long-term dynamics of the protein for both sets of simulation conditions, two Anisotropic Network Models (ANMs) were parametrized. An ANM starts from a single configuration, usually the native state of the protein. Each ANM contains two free parameters: the cutoff distance (within which residues are connected by a harmonic potential) and the global force constant (used in all harmonic potentials). The low temp (113 K) ANM was linearly fit to the crystallographic B factors of the trimer KDPG aldolase PDB file (1WA3) at a cutoff of 13 Å and a global force constant of 15.039 pN/Å. Comparison between the crystallographic B factors and the calculated B factors of the ANM match closely at 100 K (section 6). Since B factors are collected at low temperature and electron microscopy model B factors have been shown to be meaningless,[34] our high temperature (300 K) ANM required high resolution simulation data. To this end, PDB file 1WA3 was used to generate a CHARMM model of our protein for a fully atomistic simulation. Our simulation system files were generated using CHARMM-GUI[35] with the CHARMM-36 force field[36] and TIP3P water molecules. After relaxation and equilibration, our system was simulated for 10 ns at 300 K using GROMACS.[37] The B factors of the C-Alpha carbons from our fully atomistic simulation were then used to parametrize our high temp ANM at a cutoff of 13 Å and a global force constant of 15.982 pN/ Å. The fully atomistic B factors from simulation and the calculated B factors of the high temp ANM fit well at 300 K (section 6).

Linker Parameterization. The DBCO-based linkers used experimentally to conjugate the KDPG aldolase to DNA were previously modeled by fitting the length distribution observed in the fully atomistic simulation of the linker to a spring potential.[22] A molecular schematic of the linker and the spring potential parameters are included in section S7.

Relaxation Procedure. First all linkers and ANMs were added to each simulation topology via the oxView design tool. Each system was then exported for simulation and subjected to a short Monte Carlo sampling (to remove any excluded volume clashes) and then a MD simulation (1×10^8 steps) with external forces enforcing the designed DNA base pairing to relax each structure into the ANM-oxDNA force field. Another MD simulation (1×10^8 steps) was performed without the forces enforcing the DNA base pairing to allow each system to equilibrate.

ASSOCIATED CONTENT

Supporting Information

The Supporting Information is available free of charge at https://pubs.acs.org/doi/10.1021/acsnano.2c04013.

KDPG aldolase protein−DNA conjugate synthesis and characterization; sequences, designs, and characterization of tetrahedral origami and four-turn tetrahedron; experimental protocols for TEM, cryo-TEM, and AFM; processing of cryo-EM data; experimental details of the fluorophore assay; anisotropic network model fitting and linker parameters; additional simulation data from the oxDNA2 model; tables of cryo-fitting data and maps; additional figures including CADNANO design scheme, agarose gel characterization, SEM and cryo-EM images, Fourier-shell correlation plots, line diagram and sequences, AFM inages, and yield bar graphs; a list of DNA sequences (PDF)

AUTHOR INFORMATION

Corresponding Authors

Po- Lin Chiu − *School of Molecular Sciences and Center for Applied Structural Discovery, The Biodesign Institute, Arizona State University, Tempe, Arizona 85287, United States*; Email: plchiu@asu.edu

Nicholas Stephanopoulos − *School of Molecular Sciences and Center for molecular design and biomimetics, The Biodesign*

https://doi.org/10.1021/acsnano.2c04013
ACS Nano 2022, 16, 14086−14096

Institute, Arizona State University, Tempe, Arizona 85287, United States; orcid.org/0000-0001-7859-410X; Email: nstepha1@asu.edu

Petr Šulc − *School of Molecular Sciences and Center for molecular design and biomimetics, The Biodesign Institute, Arizona State University, Tempe, Arizona 85287, United States;* orcid.org/0000-0003-1565-6769; Email: psulc@asu.edu

Authors

Raghu Pradeep Narayanan − *School of Molecular Sciences and Center for molecular design and biomimetics, The Biodesign Institute, Arizona State University, Tempe, Arizona 85287, United States;* Present Address: Department of Cellular and Molecular Pharmacology, University of California, San Francisco, California 94143, USA

Jonah Procyk − *School of Molecular Sciences and Center for molecular design and biomimetics, The Biodesign Institute, Arizona State University, Tempe, Arizona 85287, United States*

Purbasha Nandi − *School of Molecular Sciences and Center for Applied Structural Discovery, The Biodesign Institute, Arizona State University, Tempe, Arizona 85287, United States*

Abhay Prasad − *School of Molecular Sciences and Center for molecular design and biomimetics, The Biodesign Institute, Arizona State University, Tempe, Arizona 85287, United States*

Yang Xu − *Center for molecular design and biomimetics, The Biodesign Institute, Arizona State University, Tempe, Arizona 85287, United States*

Erik Poppleton − *Center for molecular design and biomimetics, The Biodesign Institute, Arizona State University, Tempe, Arizona 85287, United States;* orcid.org/0000-0002-5146-5970

Dewight Williams − *Eyring Materials Center, Office of Knowledge Enterprise Development, Arizona State University, Tempe, Arizona 85287, United States*

Fei Zhang − *Department of Chemistry, Rutgers University, Newark, New Jersey 07102, United States;* orcid.org/0000-0002-3177-7547

Hao Yan − *School of Molecular Sciences and Center for molecular design and biomimetics, The Biodesign Institute, Arizona State University, Tempe, Arizona 85287, United States;* orcid.org/0000-0001-7397-9852

Complete contact information is available at: https://pubs.acs.org/10.1021/acsnano.2c04013

Author Contributions

The manuscript was written through contributions of all authors. All authors have given approval to the final version of the manuscript.

Author Contributions

[▽]R.P.N. and J.P. contributed equally as first authors.

Author Contributions

[#]P.N., A.P., and Y.X. contributed equally as second authors.

Funding

NSF Grant no 1931487. NSF Grant no 1753387. NIH Grant DP2GM132931. DOE grant DE-SC0002423. ONR Grant N000142012094. NSF MRI Grant 1531991.

Notes

The authors declare no competing financial interest.

The structures designed in this work are available at no charge via nanobase.org, an online repository of nanostructures.[26]

ACKNOWLEDGMENTS

This work was supported by NSF Grant no 1931487 and ONR Grant N000142012094. Nicholas Stephanopoulos acknowledges support from the National Science Foundation (DMR-BMAT CAREER award 1753387). Research reported in this publication was supported by The National Institute of General Medical Sciences of the National Institutes of Health under grant number DP2GM132931. The content is solely the responsibility of the authors and does not necessarily represent the official views of the National Institutes of Health. Po-Lin Chiu acknowledges the support from the US Department of Energy (DE-SC0002423).

ABBREVIATIONS

PDNA, protein−DNA hybrid building block; DNA, deoxyribonucleic acid; TEM, transmission electron microscopy; AFM, atomic force microscopy; PDTet, four-turn protein−DNA tetrahedron; KDPG aldolase, 2-dehydro-3-deoxy-phosphogluconate aldolase; ANM, anisotropic network model

REFERENCES

(1) Krishnan, Y.; Seeman, N. C. Introduction: Nucleic Acid Nanotechnology. *Chem. Rev.* **2019**, *119* (10), 6271−6272.

(2) Hong, F.; Zhang, F.; Liu, Y.; Yan, H. DNA Origami: Scaffolds for Creating Higher Order Structures. *Chem. Rev.* **2017**, *117* (20), 12584−12640.

(3) Watson, J. D.; Crick, F. H. C. Molecular Structure of Nucleic Acids: A Structure for Deoxyribose Nucleic Acid. *Nature* **1953**, *171* (4356), 737−738.

(4) Chen, K.; Kong, J.; Zhu, J.; Ermann, N.; Predki, P.; Keyser, U. F. Digital Data Storage Using DNA Nanostructures and Solid-State Nanopores. *Nano Lett.* **2019**, *19* (2), 1210−1215.

(5) Chen, K.; Zhu, J.; Bošković, F.; Keyser, U. F. Nanopore-Based DNA Hard Drives for Rewritable and Secure Data Storage. *Nano Lett.* **2020**, *20* (5), 3754−3760.

(6) Song, T.; Eshra, A.; Shah, S.; Bui, H.; Fu, D.; Yang, M.; Mokhtar, R.; Reif, J. Fast and compact DNA logic circuits based on single-stranded gates using strand-displacing polymerase. *Nat. Nanotechnol.* **2019**, *14* (11), 1075−1081.

(7) Qian, L.; Winfree, E. Scaling Up Digital Circuit Computation with DNA Strand Displacement Cascades. *Science* **2011**, *332* (6034), 1196−1201.

(8) Seelig, G.; Soloveichik, D.; Zhang, D. Y.; Winfree, E. Enzyme-Free Nucleic Acid Logic Circuits. *Science* **2006**, *314* (5805), 1585−1588.

(9) Thubagere, A. J.; Thachuk, C.; Berleant, J.; Johnson, R. F.; Ardelean, D. A.; Cherry, K. M.; Qian, L. Compiler-aided systematic construction of large-scale DNA strand displacement circuits using unpurified components. *Nat. Commun.* **2017**, *8* (1), 14373.

(10) Li, S.; Jiang, Q.; Liu, S.; Zhang, Y.; Tian, Y.; Song, C.; Wang, J.; Zou, Y.; Anderson, G. J.; Han, J.-Y.; Chang, Y.; Liu, Y.; Zhang, C.; Chen, L.; Zhou, G.; Nie, G.; Yan, H.; Ding, B.; Zhao, Y. A DNA nanorobot functions as a cancer therapeutic in response to a molecular trigger in vivo. *Nat. Biotechnol.* **2018**, *36* (3), 258−264.

(11) Jiang, Q.; Song, C.; Nangreave, J.; Liu, X.; Lin, L.; Qiu, D.; Wang, Z.-G.; Zou, G.; Liang, X.; Yan, H.; Ding, B. DNA Origami as a Carrier for Circumvention of Drug Resistance. *J. Am. Chem. Soc.* **2012**, *134* (32), 13396−13403.

(12) Huang, P. S.; Boyken, S. E.; Baker, D. The coming of age of de novo protein design. *Nature* **2016**, *537* (7620), 320−7.

(13) Das, R.; Baker, D. Macromolecular Modeling with Rosetta. *Annu. Rev. Biochem.* **2008**, *77* (1), 363−382.

(14) Hu, Q.; Li, H.; Wang, L.; Gu, H.; Fan, C. DNA Nanotechnology-Enabled Drug Delivery Systems. *Chem. Rev.* **2019**, *119* (10), 6459−6506.
(15) Douglas, S. M.; Bachelet, I.; Church, G. M. A Logic-Gated Nanorobot for Targeted Transport of Molecular Payloads. *Science* **2012**, *335* (6070), 831−834.
(16) Jin, J.; Baker, E. G.; Wood, C. W.; Bath, J.; Woolfson, D. N.; Turberfield, A. J. Peptide Assembly Directed and Quantified Using Megadalton DNA Nanostructures. *ACS Nano* **2019**, *13* (9), 9927−9935.
(17) Buchberger, A.; Simmons, C. R.; Fahmi, N. E.; Freeman, R.; Stephanopoulos, N. Hierarchical Assembly of Nucleic Acid/Coiled-Coil Peptide Nanostructures. *J. Am. Chem. Soc.* **2020**, *142* (3), 1406−1416.
(18) Williams, S.; Lund, K.; Lin, C.; Wonka, P.; Lindsay, S.; Yan, H. In *Tiamat: A Three-Dimensional Editing Tool for Complex DNA Structures, DNA Computing*; Goel, A.; Simmel, F. C.; Sosík, P., Eds.; Springer Berlin Heidelberg: Berlin, Heidelberg, 2009; pp 90−101.
(19) Douglas, S. M.; Marblestone, A. H.; Teerapittayanon, S.; Vazquez, A.; Church, G. M.; Shih, W. M. Rapid prototyping of 3D DNA-origami shapes with caDNAno. *Nucleic Acids Res.* **2009**, *37* (15), 5001−5006.
(20) de Llano, E.; Miao, H.; Ahmadi, Y.; Wilson, A. J.; Beeby, M.; Viola, I.; Barisic, I. Adenita: interactive 3D modelling and visualization of DNA nanostructures. *Nucleic Acids Res.* **2020**, *48* (15), 8269−8275.
(21) Huang, C.-M.; Kucinic, A.; Johnson, J. A.; Su, H.-J.; Castro, C. E. Integrated computer-aided engineering and design for DNA assemblies. *Nat. Mater.* **2021**, *20* (9), 1264−1271.
(22) Lu, W.; Bueno, C.; Schafer, N. P.; Moller, J.; Jin, S.; Chen, X.; Chen, M.; Gu, X.; Davtyan, A.; de Pablo, J. J.; Wolynes, P. G. OpenAWSEM with Open3SPN2: A fast, flexible, and accessible framework for large-scale coarse-grained biomolecular simulations. *PLoS Comput. Biol.* **2021**, *17* (2), No. e1008308.
(23) Xu, Y.; Jiang, S.; Simmons, C. R.; Narayanan, R. P.; Zhang, F.; Aziz, A.-M.; Yan, H.; Stephanopoulos, N. Tunable Nanoscale Cages from Self-Assembling DNA and Protein Building Blocks. *ACS Nano* **2019**, *13* (3), 3545−3554.
(24) Procyk, J.; Poppleton, E.; Šulc, P. Coarse-grained nucleic acid-protein model for hybrid nanotechnology. *Soft Matter* **2021**, *17* (13), 3586−3593.
(25) Poppleton, E.; Bohlin, J.; Matthies, M.; Sharma, S.; Zhang, F.; Šulc, P. Design, optimization and analysis of large DNA and RNA nanostructures through interactive visualization, editing and molecular simulation. *Nucleic Acids Res.* **2020**, *48* (12), e72−e72.
(26) Poppleton, E.; Mallya, A.; Dey, S.; Joseph, J.; Šulc, P. Nanobase.org: a repository for DNA and RNA nanostructures. *Nucleic Acids Res.* **2022**, *50* (D1), D246−D252.
(27) Lyumkis, D. Challenges and opportunities in cryo-EM single-particle analysis. *J. Biol. Chem.* **2019**, *294* (13), 5181−5197.
(28) Šulc, P.; Romano, F.; Ouldridge, T. E.; Rovigatti, L.; Doye, J. P. K.; Louis, A. A. Sequence-dependent thermodynamics of a coarse-grained DNA model. *J. Chem. Phys.* **2012**, *137* (13), 135101.
(29) Doye, J. P. K.; Ouldridge, T. E.; Louis, A. A.; Romano, F.; Šulc, P.; Matek, C.; Snodin, B. E. K.; Rovigatti, L.; Schreck, J. S.; Harrison, R. M.; Smith, W. P. J. Coarse-graining DNA for simulations of DNA nanotechnology. *Phys. Chem. Chem. Phys.* **2013**, *15* (47), 20395−20414.
(30) Snodin, B. E. K.; Randisi, F.; Mosayebi, M.; Šulc, P.; Schreck, J. S.; Romano, F.; Ouldridge, T. E.; Tsukanov, R.; Nir, E.; Louis, A. A.; Doye, J. P. K. Introducing improved structural properties and salt dependence into a coarse-grained model of DNA. *J. Chem. Phys.* **2015**, *142* (23), 234901.
(31) Srinivas, N.; Ouldridge, T. E.; Šulc, P.; Schaeffer, J. M.; Yurke, B.; Louis, A. A.; Doye, J. P. K.; Winfree, E. On the biophysics and kinetics of toehold-mediated DNA strand displacement. *Nucleic Acids Res.* **2013**, *41* (22), 10641−10658.
(32) Suma, A.; Poppleton, E.; Matthies, M.; Šulc, P.; Romano, F.; Louis, A. A.; Doye, J. P. K.; Micheletti, C.; Rovigatti, L. TacoxDNA: A user-friendly web server for simulations of complex DNA structures, from single strands to origami. *J. Comput. Chem.* **2019**, *40* (29), 2586−2595.
(33) Pettersen, E. F.; Goddard, T. D.; Huang, C. C.; Couch, G. S.; Greenblatt, D. M.; Meng, E. C.; Ferrin, T. E. UCSF Chimera-a visualization system for exploratory research and analysis. *J. Comput. Chem.* **2004**, *25* (13), 1605−12.
(34) Wlodawer, A.; Li, M.; Dauter, Z. High-Resolution Cryo-EM Maps and Models: A Crystallographer's Perspective. *Structure* **2017**, *25* (10), 1589−1597.
(35) Jo, S.; Kim, T.; Iyer, V.; Im, W. CHARMM-GUI: a web-based graphical user interface for CHARMM. *J. Comput. Chem.* **2008**, *29*, 1859−65.
(36) Huang, J.; MacKerell Jr, A. D. CHARMM36 all-atom additive protein force field: Validation based on comparison to NMR data. *J. Comput. Chem.* **2013**, *34* (25), 2135−2145.
(37) Abraham, M. J.; Murtola, T.; Schulz, R.; Páll, S.; Smith, J. C.; Hess, B.; Lindahl, E. GROMACS: High performance molecular simulations through multi-level parallelism from laptops to supercomputers. *SoftwareX* **2015**, *1−2*, 19−25.
(38) Poppleton, E.; Mallya, A.; Dey, S.; Joseph, J.; Šulc, P. Nanobase.org: a repository for DNA and RNA nanostructures. *Nucleic Acids Res.* **2022**, *50* (D1), D246−D252.

https://doi.org/10.1021/acsnano.2c04013
ACS Nano 2022, 16, 14086−14096